

# Long range pure magnon spin diffusion observed in a non-local spin-Seebeck geometry

Brandon L. Giles<sup>1</sup>, Zihao Yang<sup>2</sup>, John Jamison<sup>1</sup>, and Roberto C. Myers<sup>1-3</sup>

<sup>1</sup>*Department of Materials Science and Engineering, The Ohio State University, Columbus, OH, 43210, USA*

*Email: [myers.1079@osu.edu](mailto:myers.1079@osu.edu), Web site: <http://myersgroup.engineering.osu.edu>*

<sup>2</sup>*Department of Electrical and Computer Engineering, The Ohio State University, Columbus, OH, 43210, USA*

<sup>3</sup>*Department of Physics, The Ohio State University, Columbus, OH, USA*

**Spin currents consist of a flux of angular momentum<sup>1</sup>. They are carried in solids by electrons in conductors, as well as by magnetic excitations (magnons) in magnetically ordered materials. The former are at the heart of the field of spin-based electronics, spintronics<sup>2</sup>, while the latter are used in magnonics<sup>3</sup>, which are logical circuits that utilize spin-wave transport. Although they are typically excited using microwaves<sup>4</sup>, the thermal generation of magnon spins<sup>5</sup> opens the appealing possibility for spin-wave devices powered by waste-heat. Despite observation of heat→spin conversion in a variety of materials via the spin-Seebeck effect<sup>6-9</sup>, the length scale of thermally excited magnon spins was not yet observed. Here we demonstrate a non-local measurement of spin-Seebeck probing the diffusion length of magnon spins in the insulating ferrimagnet yttrium iron garnet (YIG). Remarkably, magnon spins are robust against inelastic scattering, with a spin diffusion length greatly exceeding the magnon thermal mean free path. The spin diffusion length for magnon spins in YIG (~47 μm at 23 K) is far larger than that of even n-GaAs<sup>10</sup>, the best**

**known electron spin conductor. Based on these results, we envision thermally-powered spintronic devices based on electrically insulating, but spin conducting materials.**

The simplest method to produce a spin current is to drive a charge current in a spin-polarized conductor, like a ferromagnetic metal. In that case, a spin current flows parallel with the charge current<sup>1</sup>. Pure spin currents, on the other hand, flow in the absence of electrical currents and can be generated using the spin Hall effect<sup>2</sup> which converts a charge current into a spin current. Laterally flowing spin currents are proposed to be used in spin current based devices where they can operate on magnetic elements via the spin torque effect<sup>11</sup>.

In the case of magnon based spin currents, a great amount of research has been performed using microwave excitation in YIG, taking advantage of the low damping rate of GHz frequency magnons in this material. Surface spin-waves in YIG can be measured using microwave electronics, resonance, or by measuring the associated spin current. Their dispersions can be engineered using artificial magnonic crystals, and recently an all-magnon based transistor was demonstrated<sup>12</sup>. Such microwave excited spin-waves are proposed for spin-wave logic devices with low power consumption<sup>13</sup>.

While magnonic spin currents can be generated using resonant microwave excitation, they can also be incoherently produced from heat. By generating spin current densities nearly two orders of magnitude larger than those produced by preexisting methods<sup>14</sup>, the spin-Seebeck effect has inspired innovative ideas in the areas of waste heat recovery<sup>15</sup> and has catalyzed the field of spin caloritronics<sup>16</sup>. In the spin-Seebeck effect, heat flow in a spin-polarized solid leads to a spin accumulation and associated spin current flowing into a non-spin-polarized material. In YIG, the spin current is carried by magnons, however these thermally-excited magnons should have much higher energies (100-6000 GHz) than the microwave (<10 GHz) magnons.

Consequently, the thermally-generated magnons are expected to couple more strongly to the lattice leading to short thermalization times and length scales far shorter than those of the microwave magnons. Despite the shorter length scales expected, thermally-excited spin currents have stimulated a great interest within the field of spin caloritronics because they open the door to spin-based devices powered by waste heat. Additionally, fundamentally new physics is predicted, such as the condensation of superfluid magnons at the Pt/YIG interface<sup>17</sup> that may lead to extraordinary spin-mediated thermal properties. However, design of experiments to realize a thermally generated magnon BEC are hampered by the lack of quantitative measurements of the length scale of magnon spins. This motivates us to measure the diffusion length of thermally-excited magnon spins.

Previously, the spin-Seebeck effect has been measured in two geometries, the transverse<sup>6,7,9</sup> and the longitudinal<sup>8</sup>. In the former, the spin current ( $\mathbf{J}_S$ ) is detected in a direction perpendicular to an applied thermal gradient ( $\mathbf{J}_S \perp \nabla T$ ), whereas in the latter,  $\mathbf{J}_S \parallel \nabla T$ . Recently, the longitudinal spin-Seebeck effect was studied as a function of YIG thin film thickness. The observed saturation of the spin-Seebeck signal for films greater than 100-nm thickness was interpreted to indicate the length scale over which magnons contribute to the signal.<sup>18</sup> However, the strong interface sensitivity of spin-Seebeck<sup>19</sup> leads to measurement uncertainty due to sample to sample variation. Additionally, in the longitudinal spin-Seebeck geometry, the applied heat flows directly into the spin detector allowing for the possibility of contaminating signals from charge-based thermo-electric effects rather than the pure spin signal<sup>20</sup>.

Here we measure the length scale of pure magnon spin diffusion in YIG in a systematic manner, while controlling for interface sensitivity. This is accomplished by utilizing a non-local detection geometry to sample spin currents induced by the spin-Seebeck effect. In metals and in

semiconductors, the non-local geometry has been successfully employed to generate and measure pure electron spin currents diffusing in the absence of an applied electric field<sup>21</sup>. Recently, electron spin currents driven by a non-local thermal excitation were also realized to detect the spin-dependent Seebeck effect<sup>22</sup>. By utilizing a non-local spin injection/detection geometry, pure magnonic spin currents are spatially isolated from the applied thermal gradient, automatically removing parasitic signals and allowing for the measurement of the magnon spin diffusion length in YIG.

Thermal spin injection and detection is performed utilizing the opto-thermal method<sup>23</sup> in which a focused laser is absorbed by a Pt film on YIG. The laser is modulated with an optical chopper and the resulting transverse voltage is sampled using a lock-in amplifier (see Methods). Instead of using a continuous Pt film, we pattern the film into a central Pt spin detector strip wired to the lock-in amplifier together with an array of electrically and spatially isolated Pt absorption pads shown schematically in Figure 1a (see Methods for processing details). When the focused laser spot is positioned on an absorption pad, a local hot spot is produced generating a thermal gradient ( $\nabla T$ ) whose magnitude is varied by adjusting the average power of the beam.  $\nabla T$  excites magnons in the YIG beneath the absorption pad leading to a spin current. Magnon spins that have laterally diffused underneath the spin detector can then vertically diffuse into the spin detector, where they are converted into an electron spin current ( $J_z^s$ ), which is, in turn, converted into a transverse voltage along the y-direction ( $V_{ISHE}$ ) by the inverse spin Hall effect (ISHE)<sup>6</sup>. The magnitude of  $V_{ISHE}$  is proportional to the spin current magnitude. The sign of  $V_{ISHE}$  tracks the sign of the spin polarization injected into the detector, and thereby follows the sign of the in-plane (xy-plane) magnetization ( $\mathbf{M}$ ) of YIG.

To ensure non-local detection of thermally-induced spin currents, no significant heat flow should occur across the interface between the spin detector and the spin source. A finite-element method (FEM) is used to simulate heat flow and steady-state temperature gradient profiles to establish the spatial extent of heat flow and define regions of thermally-driven versus purely-diffusive magnonic spin currents in YIG (see Methods). When exposed to a focused laser beam, there is heat flow both in the vertical and lateral direction beneath the absorption pad, characterized by the thermal gradients  $\nabla T_z$  and  $\nabla T_x$ , respectively. Both  $\nabla T_z$  and  $\nabla T_x$  from FEM simulations are plotted in Figure 1b and c at 23 K using an average laser power of 29.9 mW and a spot diameter of 7.5  $\mu\text{m}$ . Clearly, in the non-local configuration, heat flows from the absorber into the YIG. Lateral heat spreading in the YIG leads to heat flow beneath ( $\nabla T_x$ ) the detector. However, because the detector is a thermal open circuit, the laterally diffusing heat cannot then diffuse vertically into the detector (see Methods). The modeled vertical temperature gradient ( $\nabla T_z$ ) at the edge of the spin detector is plotted in Figure 1d.  $\nabla T_z$  is only present when the laser is absorbed by the detector, and can be neglected whenever the laser is not focused on the spin detector.  $\nabla T_x$  at the edge of the spin detector decays to 1% of its peak value after the laser is displaced  $22.9 \pm 1.08 \mu\text{m}$  from the detector. Therefore, spin currents measured within 23  $\mu\text{m}$  of the detector may be driven by lateral heat flow even if no heat flows vertically into the detector. When the laser is positioned at a distance greater than 23  $\mu\text{m}$ , there is neither substantial vertical nor lateral heat flow beneath the detector. We therefore define three thermal zones. In zone I, heat flows vertically through the spin detector. Since  $\nabla T_z$  is present, then within this zone the longitudinal<sup>8</sup> ( $\nabla T_z$  driven) spin-Seebeck effect is expected to contribute to  $V_{ISHE}$ . However,  $\nabla T_x$  is cancelled by circular symmetry, therefore transverse<sup>7</sup> ( $\nabla T_x$  driven) spin-Seebeck effect is not expected. Additionally, within this zone  $\nabla T_z$  can generate a transverse voltage ( $V_y$ ) that tracks the

sign and magnitude of the x-component of the in-plane magnetization of YIG ( $M_x$ ) due to the anomalous Nernst effect (ANE)<sup>24</sup>, which can occur in Pt/YIG<sup>25</sup>. In zone II, there is no longer heat flow into the spin detector (negligible  $\nabla T_z$ ) therefore ANE or other thermal parasitic signals cannot occur in the spin detector. On the other hand, a  $\nabla T_x$  is present, therefore the transverse spin-Seebeck effect is possible, i.e. magnon spins may be laterally driven by  $\nabla T_x$ . Finally, in zone III, neither  $\nabla T_z$  nor  $\nabla T_x$  are significant, therefore only purely diffusive magnon spins reach the detector.

In Figure 2, raw voltage traces are shown as a function of an applied in-plane magnetic field ( $B_x$ ) for measurements carried out with the laser positioned in two different regions. If the laser is positioned directly on the Pt detection strip (zone I), the spin current is measured locally, and thereby may contain contributions from longitudinal spin-Seebeck as well as ANE. This configuration is shown in Figure 2a. The raw transverse voltage ( $V_y$ ) across the Pt detection strip is presented in Figure 2b as a function of  $B_x$ . The transverse voltage saturates to  $746 \pm 3$  nV at  $>|50|$  mT, which matches the saturation field of YIG, and the sharp  $V_y$  hysteresis is consistent with the small coercive field of YIG. The M-B curve for this sample is included in Fig. 2b for comparison. We define the magnitude of the local voltage ( $V_L$ ) as the magnitude of the hysteresis loop, averaging the amplitude of the saturation voltage at positive and negative fields. The inset plots  $V_L$  over the range of laser powers measured revealing the linear relationship consistent with both the SSE and ANE dependence on  $\nabla T_z$ . Note that in the absence of additional measurements<sup>26</sup> it is not possible in the local configuration to determine the magnitude of the ANE<sup>25</sup> ( $V_{ANE}$ ) versus the magnitude of the spin current induced ISHE ( $V_{ISHE}$ ), that is,  $V_L = V_{ANE} + V_{ISHE}$ . In the second configuration, the laser is positioned on one of the electrically isolated Pt absorption pads to measure the spin-current non-locally, as depicted in Figure 2c.

Since there is no heat flow across the detector ( $\nabla T_z = 0$ ), then ANE cannot contribute and the non-local configuration allows detection of only the thermally-induced magnonic spin current, i.e.  $V_{ANE} = 0$ . Figure 2d shows the corresponding raw  $V_y$  in the Pt detection strip as a function of  $B_x$  if the laser is positioned on an absorption pad whose center is 8  $\mu\text{m}$  from the detection pad edge (zone II). Again, the transverse voltage tracks the magnetic hysteresis of YIG. The magnitude of the non-local voltage ( $V_{NL}$ ) is defined as above, but no longer contains any possible ANE contribution, therefore  $V_{NL} = V_{ISHE}$ . It scales linearly with laser power, however its overall intensity is an order of magnitude smaller than what is observed in the local configuration ( $V_L$ ).

To spatially map the thermally-generated magnonic spin current,  $V_{ISHE}$  is extracted from raw hysteresis traces (as in Figure 2) with the laser positioned above absorption pads at increasing distances from the spin detector. Figure 3a plots  $V_{ISHE}$  extracted from such measurements plotted as a function of laser position from the edge of the spin detector ( $\Delta x$ ). The same measurement is carried out at three different laser powers and the thermal zones are color coded as in Figure 1d. Additionally, the modeled  $\nabla T_x$  at each of the three laser powers is plotted in Figure 3a to compare the spin transport versus the thermal transport. Since non-negligible  $\nabla T_x$  is present at the edge of the spin detector in zone II, then in this region magnon spins might be thermally-driven by the transverse spin-Seebeck effect. To examine this possibility the data are fit to a single decaying exponential over various ranges (see Methods). There is no significant variation for fits carried out over zones II and III versus those confined to zone III alone. Additionally,  $\nabla T_x$  decays much more rapidly than  $V_{ISHE}$ . This indicates that the lateral heat flow appears to have negligible impact on the non-local magnon spin measurements, at least in their current configuration. The lack of  $\nabla T_x$  driven effect (transverse spin-Seebeck) may be a result of  $\nabla T_x$  decaying very quickly beneath the interface, whereas in transverse spin-Seebeck

experiments a uniform  $\nabla T_x$  is applied leading to uniform heat flow throughout the entire thickness of the sample. Regardless, the current non-local measurements reflect the magnitude of the purely diffusive magnonic spin current detected in the absence of heat flow (zone III). The spin current decays exponentially with distance, consistent with the solution to the spin-diffusion equation at steady-state. From the exponential fits,  $V_{ISHE}(\Delta x) = V_{ISHE}^s e^{-\Delta x/\lambda_s}$ , we obtain the contribution of the purely magnonic spin current ( $V_{ISHE}^s$ ) to the measured  $V_{ISHE}$  as well as the magnon spin diffusion length  $\lambda_s$  (solid lines in Figure 3a).

The magnon spin diffusion lengths are plotted in Figure 3b as a function of laser power revealing an average value of 47  $\mu\text{m}$  independent of laser power. The lack of a change in the diffusion length with laser power implies that the magnon spin scattering and lifetime are insensitive to the applied temperature gradient. The amplitudes are plotted in Figure 3c comparing the purely diffusive spin current ( $V_{ISHE}^s$ ) and the locally detected transverse voltage ( $V_L$ ). These amplitudes scale linearly with laser power implying the measurements are well within the linear regime of spin-heat transport. Interestingly, the purely magnonic spin current accounts for only a very small fraction of the transverse voltage measured under local conditions (Figure 2a), where  $V_L = 746 \pm 3$  nV.

We now compare the diffusion of magnon spins in YIG with the diffusion of magnon heat. Recently, Boona and Heremans examined the thermal conductivity of bulk YIG as a function of temperature and magnetic field to extract the thermal conductivity of magnons<sup>27</sup>. Together with heat capacity measurements, they calculated the expected thermal mean free path for magnons ( $l_T$ ) as a function of temperature, and it was found that  $l_T = 4$   $\mu\text{m}$  at 20 K. Note that this mean free path reflects that of the magnons responsible for thermal transport, i.e. those magnons that contribute to the thermal conductivity of YIG. Therefore  $l_T$  reflects the distance

between inelastic scattering events. On the other hand, our measurements demonstrate that at the same temperature, magnon spins diffuse more than one order of magnitude larger distances ( $\lambda_S = 47 \mu\text{m}$ ).

Two explanations are offered for the observation that  $\lambda_S \gg l_T$  for magnons in YIG. First, taken at face value, magnons retain their spin even after multiple inelastic scattering events. In that view, the long range magnons being detected are cooled magnons that still carry spin. This simple picture mirrors the case for electron spins in solids, where the spin-flip rate of electrons is typically far slower than the charge scattering rate. Thus, like electrons, magnons retain their spin polarization between successive linear momentum scattering events. In the second view, during thermal excitation of YIG the thermal magnons that carry the majority of the heat scatter at short distances due to their short wavelengths and stronger interaction with the lattice. However, a small subset of the magnons at much lower energies, called sub-thermal magnons with longer wavelengths, do not couple effectively to the lattice and therefore exhibit much longer mean free paths. As recently suggested<sup>27</sup>, this can explain the  $\sim 100$  nm length scale of longitudinal spin-Seebeck effect at room temperature<sup>18</sup>, the high magnetic field suppression of spin-Seebeck at room temperature<sup>28,29</sup> and is also consistent with our current observations at low temperature.

Since thermally-induced magnon spins in YIG are preserved over tens of microns, they may be used in laterally-patterned spin-current based devices powered by waste-heat. The low temperature magnon spin diffusion length of YIG is, in fact, far longer than that of n-GaAs ( $\sim 6 \mu\text{m}$  at 4.2 K), the best known electron spin conductor<sup>10</sup>. It is therefore worthwhile to consider using magnon spin conductors as the lateral spin channels (spin interconnects) in existing spin-based device proposals<sup>11</sup>. Consider, for example, an alternative configuration of the all-spin-

logic-device, where the non-locally generated spin currents are carried by magnons in an electrically insulating material. In this configuration, the device is powered by thermal gradients that excite magnonic spin currents without any charge currents. However, it is not obvious that YIG is the ideal material for thermal production of magnon spin currents. Therefore, much work remains to examine thermally-induced magnon spin transport in other solids. The material selection need not be restricted to ferro and ferrimagnets as insulating antiferromagnets, like NiO, also exhibit significant spin wave conductivity<sup>30</sup>. Additionally, at higher excitation densities, non-linear spin-thermal effects, such as dynamical magnon BEC<sup>17</sup> may yield significantly greater spin current magnitudes and open the door to thermally-driven coherent spin-wave devices.

## References:

1. Žutić, I., Fabian, J. & Das Sarma, S. Spintronics: Fundamentals and applications. *Rev. Mod. Phys.* **76**, 323–410 (2004).
2. Awschalom, D. D. & Flatté, M. E. Challenges for semiconductor spintronics. *Nat. Phys.* **3**, 153–159 (2007).
3. Neusser, S. & Grundler, D. Magnonics: Spin Waves on the Nanoscale. *Adv. Mater.* **21**, 2927–2932 (2009).
4. Eshbach, J. R. Spin-Wave Propagation and the Magnetoelastic Interaction in Yttrium Iron Garnet. *Phys. Rev. Lett.* **8**, 357–359 (1962).
5. Uchida, K. *et al.* Spin Seebeck insulator. *Nat. Mater.* **9**, 894–897 (2010).
6. Uchida, K. *et al.* Observation of the spin Seebeck effect. *Nature* **455**, 778–781 (2008).
7. Jaworski, C. M. *et al.* Observation of the spin-Seebeck effect in a ferromagnetic semiconductor. *Nat. Mater.* **9**, 898–903 (2010).
8. Uchida, K. *et al.* Observation of longitudinal spin-Seebeck effect in magnetic insulators. *Appl. Phys. Lett.* **97**, 172505 (2010).
9. Jaworski, C. M., Myers, R. C., Johnston-Halperin, E. & Heremans, J. P. Giant spin Seebeck effect in a non-magnetic material. *Nature* **487**, 210–213 (2012).
10. Dzhioev, R. I. *et al.* Low-temperature spin relaxation in n-type GaAs. *Phys. Rev. B* **66**, 245204 (2002).
11. Behin-Aein, B., Datta, D., Salahuddin, S. & Datta, S. Proposal for an all-spin logic device with built-in memory. *Nat. Nanotechnol.* **5**, 266–270 (2010).
12. Chumak, A. V., Serga, A. A. & Hillebrands, B. Magnon transistor for all-magnon data processing. *Nat. Commun.* **5**, 4700 (2014).

13. Schneider, T. *et al.* Realization of spin-wave logic gates. *Appl. Phys. Lett.* **92**, 022505 (2008).
14. Weiler, M. *et al.* Experimental Test of the Spin Mixing Interface Conductivity Concept. *Phys. Rev. Lett.* **111**, 176601 (2013).
15. Kiriwara, A. *et al.* Spin-current-driven thermoelectric coating. *Nat. Mater.* **11**, 686–689 (2012).
16. Bauer, G. E. W., Saitoh, E. & van Wees, B. J. Spin caloritronics. *Nat. Mater.* **11**, 391–399 (2012).
17. Bender, S. A., Duine, R. A., Brataas, A. & Tserkovnyak, Y. Dynamic phase diagram of dc-pumped magnon condensates. *Phys. Rev. B* **90**, 094409 (2014).
18. Kehlberger, A. *et al.* Determination of the origin of the spin Seebeck effect - bulk vs. interface effects. *ArXiv13060784 Cond-Mat* (2013). at <<http://arxiv.org/abs/1306.0784>>
19. Aqeel, A., Vera-Marun, I. J., van Wees, B. J. & Palstra, T. T. M. Surface sensitivity of the spin Seebeck effect. *J. Appl. Phys.* **116**, 153705 (2014).
20. Boona, S. R., Myers, R. C. & Heremans, J. P. Spin caloritronics. *Energy Environ. Sci.* **7**, 885–910 (2014).
21. Jedema, F. J., Heersche, H. B., Filip, A. T., Baselmans, J. J. A. & van Wees, B. J. Electrical detection of spin precession in a metallic mesoscopic spin valve. *Nature* **416**, 713–716 (2002).
22. Slachter, A., Bakker, F. L., Adam, J.-P. & van Wees, B. J. Thermally driven spin injection from a ferromagnet into a non-magnetic metal. *Nat. Phys.* **6**, 879–882 (2010).
23. Weiler, M. *et al.* Local Charge and Spin Currents in Magnetothermal Landscapes. *Phys. Rev. Lett.* **108**, 106602 (2012).

24. Miyasato, T. *et al.* Crossover Behavior of the Anomalous Hall Effect and Anomalous Nernst Effect in Itinerant Ferromagnets. *Phys. Rev. Lett.* **99**, 086602 (2007).
25. Huang, S. Y. *et al.* Transport Magnetic Proximity Effects in Platinum. *Phys. Rev. Lett.* **109**, 107204 (2012).
26. Kikkawa, T. *et al.* Separation of longitudinal spin Seebeck effect from anomalous Nernst effect: Determination of origin of transverse thermoelectric voltage in metal/insulator junctions. *Phys. Rev. B* **88**, 214403 (2013).
27. Boona, S. R. & Heremans, J. P. Magnon thermal mean free path in yttrium iron garnet. *Phys. Rev. B* **90**, 064421 (2014).
28. Kikkawa, T. *et al.* Critical suppression of spin Seebeck effect by magnetic fields. *ArXiv150305764 Cond-Mat* (2015). at <<http://arxiv.org/abs/1503.05764>>
29. Jin, H., Boona, S. R., Yang, Z., Myers, R. C. & Heremans, J. P. The effect of the magnon dispersion on the longitudinal spin Seebeck effect in yttrium iron garnets (YIG). *ArXiv150400895 Cond-Mat* (2015). at <<http://arxiv.org/abs/1504.00895>>
30. Wang, H., Du, C., Hammel, P. C. & Yang, F. Antiferromagnonic Spin Transport from Y<sub>3</sub>Fe<sub>5</sub>O<sub>12</sub> into NiO. *Phys. Rev. Lett.* **113**, 097202 (2014).

## **Acknowledgements**

The authors thank J. P. Heremans and S. R. Boona for useful discussions. This work was primarily supported by the Army Research Office MURI W911NF-14-1-0016. J.J. acknowledges the Center for Emergent Materials at The Ohio State University, an NSF MRSEC (Award Number DMR-1420451), for providing partial funding for this research.

## **Author contributions**

The experiments were designed by B.L.G. and R.C.M. The samples were fabricated by Z.Y. with help from R.C.M. The measurements were carried out by B.L.G. and J.J. with help from R.C.M. Thermal modeling was performed by Z.Y. All authors discussed the results and wrote the manuscript.

## **Additional Information**

**Methods** along with additional Extended Data display items are available in the online version of the papers including a full description of COMSOL simulations, and additional optothermal spin-Seebeck measurements.

**Competing financial interests:** The authors declare no competing financial interests.

## Figures

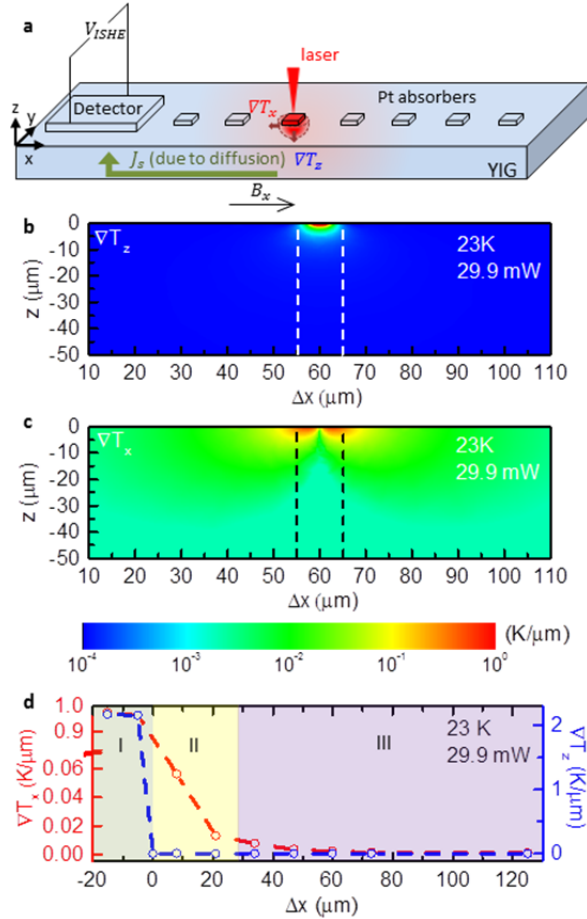


**Figure 1 | Non-local spin-Seebeck measurement geometry and modeled temperature profile with remote laser heating.** **a**, Schematic diagram of the non-local spin current injection/detection geometry (not to scale). **b** & **c**, Two-dimensional (2D) color maps of the modeled temperature gradients in the vertical direction ( $\nabla T_z$  in **b**), and the lateral direction ( $\nabla T_x$  in **c**) with the laser positioned over an absorber at  $\Delta x = 60 \mu\text{m}$  plotted as a function of distance from the edge of the detector ( $\Delta x$ ) and as a function of the depth ( $z$ ) from the surface of YIG. The edges of the absorber are indicated by dashed lines in **b** & **c** revealing that both  $\nabla T_x$  and  $\nabla T_z$  are well isolated from the edge of the spin detector (at  $\Delta x = 0 \mu\text{m}$ ). The color scale is logarithmic. **d**, Plot of the temperature gradients present at the spin detector ( $z = 0 \mu\text{m}$ , and  $\Delta x = 0 \mu\text{m}$ ) as a function of laser position ( $\Delta x$ ). Zones I, II, and III are defined in the text based on the laser-induced  $\nabla T$  components beneath the detector. Since the spin detector is a thermal open circuit, no heat flows ( $\nabla T_z = 0$ ) into the detector when the laser is absorbed remotely ( $\Delta x > 0$ ), zones II & III.

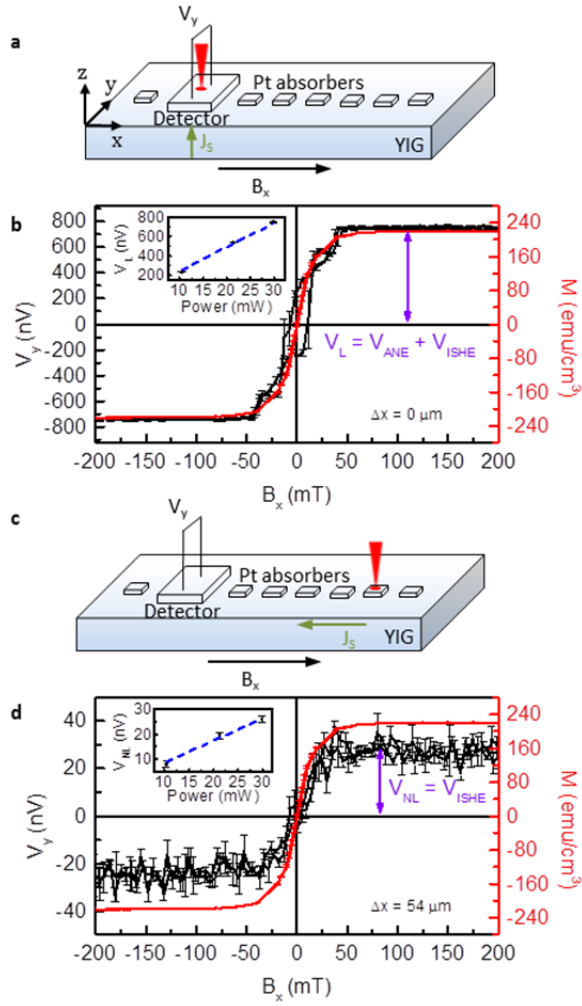


**Figure 2 | Local versus non-local detection of magnon spins in YIG at 23 K.** **a**, Schematic of the local detection geometry. **b**, The transverse voltage across the spin detector ( $V_y$ ) as a function of the applied in-plane magnetic field ( $B_x$ ) with the laser positioned on the spin detector as shown in **a**. The measured magnetization ( $M$ ) is included for comparison. The magnitude of the local voltage is defined as  $V_L$  shown in the plot and may contain components not purely due to spin currents. The inset plots  $V_L$  as a function of laser power. **c**, Schematic of the non-local spin-Seebeck geometry. **d**,  $V_y$  as a function of  $B_x$  with the laser positioned on a remote absorber as shown in **c**.  $M$  is also plotted for comparison. The magnitude of the non-local signal ( $V_{NL} = V_{ISHE}$ ) is proportional to the magnon spin current diffusing from the absorber to the detector, which is plotted in the inset as a function of laser power.

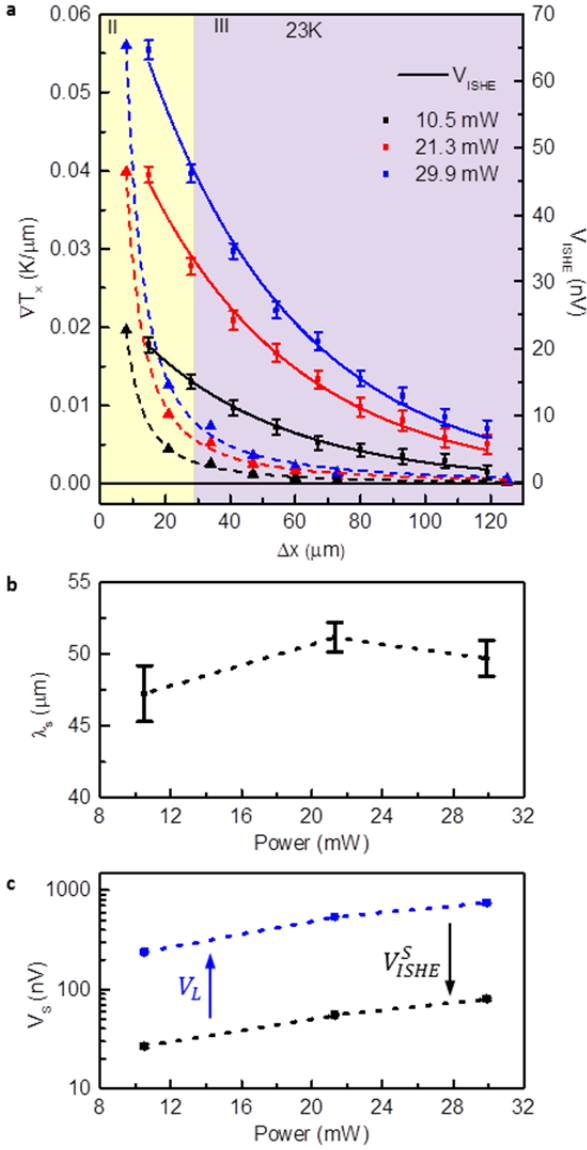


**Figure 3 | Mapping the diffusion of thermally-generated magnonic spin currents in YIG.** **a**, The magnitude of the non-local signal ( $V_{NL} = V_{ISHE}$ ) as a function of laser position from the edge of the spin detector ( $\Delta x$ ) measured with three different laser powers. The signal reveals exponential decay of the magnon spin current produced at the absorber and diffusing to the spin detector.  $\nabla T_x$  and thermal zones as defined in Figure 1d, are included for comparison (dashed lines are guides to the eye). The  $V_{ISHE}$  data are well fit to a single decaying exponential (solid lines) to obtain the pure magnon spin diffusion length ( $\lambda_S$ ) plotted in, **b**, as a function of laser power. **c**, The fit magnitude ( $V_{ISHE}^S$ ) is plotted as a function of laser power and represents the contribution of the non-local magnonic spin current to the measured  $V_{ISHE}$ . The local voltage ( $V_L$ ) taken with the laser positioned over the detector (zone I) is included for comparison.

## Methods

### Finite element Temperature Modeling (COMSOL)

Thermal modeling is carried out using the commercially available 3D FEM software COMSOL<sup>31</sup>. Three dimensional steady-state heat diffusion equations are solved in Pt/YIG bilayer structures. In the model, the YIG  $5\text{ mm} \times 5\text{ mm} \times 0.5\text{ mm}$ . The Pt spin detector is  $265\text{ }\mu\text{m} \times 265\text{ }\mu\text{m} \times 10\text{ nm}$  (center region) and the absorption pads are  $10\text{ }\mu\text{m} \times 10\text{ }\mu\text{m} \times 10\text{ nm}$ . All geometrical parameters match those of the device used in the non-local measurement. The bottom surface of the YIG is fixed at ambient temperature, mimicking the copper heat sink used in the measurement, while all other surface boundaries are thermally insulating, representing the vacuum in the cryostat. The laser is modeled as a Gaussian beam with a wavelength of 715 nm, and spot size of  $1/e^2$  radius  $r = 3.75\text{ }\mu\text{m}$ . The spot size of the laser was acquired by a knife edge measurement<sup>32</sup>.

The characteristics of the modeled laser match those of the laser employed in the measurement (width of 150 fs, 80 MHz repetition rate, modulated at a frequency of  $\sim 2\text{ kHz}$ ). As ultrafast modelling (not shown here) indicates that a quasi-steady state is reached between each ultrafast pulse, we modeled the laser beam to consist of a square-wave (in reality a train of pulses) modulated at 2 kHz. The resulting time profile of the variation of temperature of the Pt/YIG bilayer system under laser excitation is shown in Extended Data Figure 1. The laser is absorbed in the center of the detector and is incident on the Pt between 0.614 and 0.886 ms. A smoothing zone of 0.025 ms is used for the rising and falling of the laser power corresponding to a rise time of 12.5  $\mu\text{s}$ . The dark blue circles and light blue rectangles are the temporal response of the temperature along the optical axis at the Pt/YIG interface and 10  $\mu\text{m}$  beneath the interface, respectively. In both cases, the temperature rapidly saturates to the steady-state solution with a

rise time (10%~90%) of ~12.6  $\mu\text{s}$  and ~23.5  $\mu\text{s}$ , respectively. Given that the system rapidly approaches steady-state and the negligible residual excess temperature, we solve the time-independent heat diffusion equations under steady-state conditions for all of the modeling presented (Figures 1 and 3). Separate simulations are carried out for various average laser powers, including 10.5, 21.3 and 29.9 mW.

The reflectivity ( $R$ ) and absorption coefficient ( $\alpha$ ) of Pt and YIG are calculated from the complex dielectric constant  $\varepsilon = \varepsilon_1 + i\varepsilon_2$ , where, for Pt<sup>33</sup>,  $\varepsilon_1 = -16.26$  and  $\varepsilon_2 = 16.86$  and for YIG<sup>34</sup>,  $\varepsilon_1 = 4.28$  and  $\varepsilon_2 = 0$  at a wavelength of 715 nm. The values of  $R$  and  $\alpha$  are found to be 73.2% and  $78.3 \times 10^6 \text{ m}^{-1}$  for Pt and 12.1% and 0 for YIG, respectively. It should be noted that the data for Pt is acquired at 77 K, and 87 K for YIG. As  $R$  and  $\alpha$  for Pt and YIG do not vary significantly at low temperature (77 K and 87 K)<sup>35,36</sup> and room temperature (300 K)<sup>37</sup> we expect that  $R$  and  $\alpha$  for Pt and YIG at 23 K are similar to their values at 77 K. Due to the thin nature of the Pt layer, we also considered the reflected power from the Pt/YIG interface that is being re-absorbed in the Pt layer. The reflectivity of the interface is calculated using the Fresnel equation<sup>37</sup> yielding  $R_{interface} = 56\%$ . The thermal properties of Pt and YIG are acquired at 23 K while the mass density data is measured at 300 K. All physical parameters used in the simulations are listed in Extended Data Table 1.

Heat loss due to convection cooling ( $Q_{conv}^{loss}$ ) and black body radiation ( $Q_{rad}^{loss}$ ) at the boundary are estimated using the Stefan-Boltzmann law<sup>40</sup> and Newton's law<sup>40</sup>,

$$Q_{conv}^{loss} = h * A * (T_{sur} - T_{amb}) \quad (1)$$

$$Q_{rad}^{loss} = \varepsilon * \sigma * A * (T_{sur}^4 - T_{amb}^4) \quad (2)$$

where  $h$  is the heat transfer coefficient,  $A$  is the sample surface area,  $\varepsilon$  is the emissivity,  $\sigma$  is the Stefan-Boltzmann constant, and  $T_{sur}$  and  $T_{amb}$  are the temperature of the sample surface and ambient, respectively. For the heat conduction loss, as all the measurements are conducted within a cryostat with a pressure below  $4 \times 10^{-6}$  torr, the heat transfer coefficient in this case is  $h = 0 \text{ W/m}^2\text{K}$  (for vacuum)<sup>41</sup> for which the convection loss  $Q_{conv}^{loss} = 0$ . For the radiation loss, using  $\sigma = 5.67 \times 10^{-8} \text{ W/m}^2\text{K}^4$ ,  $\varepsilon_{Pt} = 7.3 \times 10^{-4}$ ,  $A = 10 \times 10 \mu\text{m}$  and  $T_{sur} = 30 \text{ K}$  (higher than the actual surface temperature on sample to estimate the upper bound of  $Q_{rad}^{loss}$ , actual  $T_{sur}$  is  $\sim 28 \text{ K}$ )<sup>42,43</sup>, we find  $Q_{rad}^{loss} \sim 10^{-12} \text{ mW}$ , which is negligible in comparison to the laser power (30 mW). Heat loss due to convection cooling and black body radiation is therefore safe to neglect in the simulations. Besides convection and radiation losses, an additional heat loss mechanism is thermal conduction along the two voltage leads (annealed Au wire) from the sample surface and is estimated by Fourier's law of thermal conduction<sup>40</sup>,

$$Q_{cond}^{loss} = \kappa * A * \nabla T \quad (3)$$

where  $\kappa$  is the thermal conductivity and  $\nabla T$  is the temperature gradient between two ends of the wire. Using  $\kappa_{Au} = 11.4 \text{ W/cmK}$ ,  $A = \pi * \left(\frac{25.4 \mu\text{m}}{2}\right)^2 = 506.7 \mu\text{m}^2$ , and  $\nabla T = \frac{30\text{K}-23\text{K}}{1 \text{ cm}} = 7 \text{ K/cm}$ , we find  $Q_{cond}^{loss} = 0.8 \text{ mW}$  which is  $\sim 3\%$  of the absorbed laser power at 30 mW<sup>44</sup>. Note that  $Q_{cond}^{loss}$  is greatly overestimated since the electrical contact between the Pt detector and the wire is spatially separated by several hundred microns from the laser heated region, therefore  $\nabla T$  will be orders of magnitude smaller than the value used in the calculation. However, even with the considerably exaggerated value,  $Q_{cond}^{loss}$  is still a small value compared to the total input power, therefore the heat loss due to the heat conduction through the wires is also neglected in the simulation, and we employ thermally insulating boundary conditions at the sample surface.

Negligible lateral heat flow is defined as when the predicted value of  $\nabla T_x$  is less than 1% of its maximum value occurring when the laser is incident on the edge of the spin detector.  $\nabla T_x$  reaches 1% of its maximum value when  $\Delta x = 22.9 \mu\text{m}$ , which defines the boundary between zone II and zone III in Figure 1.

### **Sample preparation and characterization**

Single-side-polished single-crystal  $\langle 100 \rangle$  YIG samples with dimensions of  $5 \times 5 \times 0.5 \text{ mm}^3$  are obtained commercially from the Princeton Scientific Corporation. The polished surface of the YIG is atomically flat and epi-ready with a surface roughness of 0.27 nm measured by atomic force microscopy (AFM) using a Bruker Dimension Icon AFM tool. The 10 nm Pt is e-beam evaporated on the YIG at a rate of  $0.15 \text{ \AA/s}$  using a Kurt Lesker LAB 18 deposition system with a base pressure  $< 2.5 \times 10^{-7}$  torr. Prior to the Pt deposition, the YIG samples are cleaned using solvent and DI water, followed by a five-minute dehydration bake at  $150 \text{ }^\circ\text{C}$  in atmosphere and a second one-hour in-situ bake at  $150 \text{ }^\circ\text{C}$ . There is no vacuum break between the in-situ baking and the actual Pt deposition in order to ensure a high quality Pt/YIG interface. The Pt is patterned into a  $265 \times 265 \mu\text{m}$  (center region) detection pad and  $10 \times 10 \mu\text{m}$  absorption pads with  $3 \mu\text{m}$  spacing using standard photo-lithography and  $\text{Cl}_2/\text{CF}_4$  based reactive-ion etching (RIE). (Extended Data Figure 2). The magnetic properties of the YIG sample are measured by superconducting quantum interference device (SQUID) magnetometry using a Quantum Design MPMS XL. The saturation magnetization is  $220 \text{ emu/cm}^3$  and the coercivity is  $5 \text{ Oe}$  with an in-plane magnetic field (same orientation as SSE measurement) at 20 K.

### **Opto-thermal spin-Seebeck measurement**

The Pt/YIG sample is wired with  $25.4 \mu\text{m}$  gold wire and is attached to a copper block heat sink using silver paste. All measurements are conducted in high vacuum in a customized closed cycle He cryostat coupled to an electromagnet capable of producing magnetic fields of  $\pm 0.25 \text{ T}$  at the sample. A Chameleon Ultra II Ti:Sapphire laser is focused through a reflective microscope objective, producing a  $7.5 \mu\text{m}$  diameter laser spot on the sample surface. Mechanically chopping the laser at  $2 \text{ kHz}$  to serve as a reference frequency allows the induced voltage to be measured using standard lock-in technique. Error bars are calculated based on the standard deviation of the value  $V_L$  and  $V_{NL}$  extracted from the magnetic field dependent measurements as defined in the text.

### **Analysis of Impact of $\nabla T_x$ on Magnon spin diffusion**

A single decaying exponential is fit to multiple  $V_{\text{ISHE}}$  data sets containing a varying number of data points. Fits were constructed from data sets that include  $\Delta x$  values that lie entirely within zone III, and also from data sets that contain  $\Delta x$  values from both zone II and zone III. As can be seen from Extended Data Table 3 and 4, there is no significant variation in the  $R^2$  value between fits including data points from both zones II and III and those containing data points exclusively from zone III. In addition, Extended Data Figure 3 and 4 shows that the fits lie within the error bars for single exponential decaying functions fit to  $V_{\text{ISHE}}$  values from both zones II and III. This indicates that  $\nabla T_x$  shows no measurable effect on magnon spin diffusion within the uncertainty of the experiment under the conditions used.

### **$\lambda_s$ Measurement Systematics and Reproducibility**

Additional non-local measurements are carried out for the laser positioned to the left and the right side of the Pt spin detector and results shown in Extended Data Figure 3 and 4. With only one outlying point (59  $\mu\text{m}$ ), these systematic measurements reveal almost identical values of  $\lambda_s$  ( $\sim 47$   $\mu\text{m}$ ) showing the lack of a laser power dependence or left/right asymmetry, as well as confirming the reproducibility of the experiment.

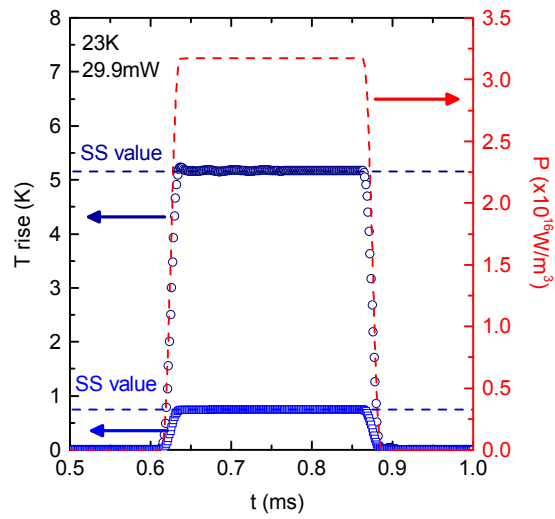
Non-local measurements are also carried out on a different Pt/YIG sample (20141004). As shown in Extended Data Figure 5, both  $V_L$  and  $V_{\text{ISHE}}$  track the magnetization. When the laser is focused on the detection pad,  $V_L$  is  $\sim 270$  nV, while when the laser is 47  $\mu\text{m}$  away,  $V_{\text{ISHE}}$  is approximately 9 nV. As the laser is moved away from the detection pad,  $V_{\text{ISHE}}$  falls off exponentially, as expected. A single decaying exponential fits the data with  $V_{\text{ISHE}}$  from both zones II and III with an adjusted  $R^2$  value of .998 (Extended Data Table 2).  $\lambda_s$  is constant regardless of the relative laser position (left side versus right side of the spin detector) shown in Extended Data Figure 6.

## References:

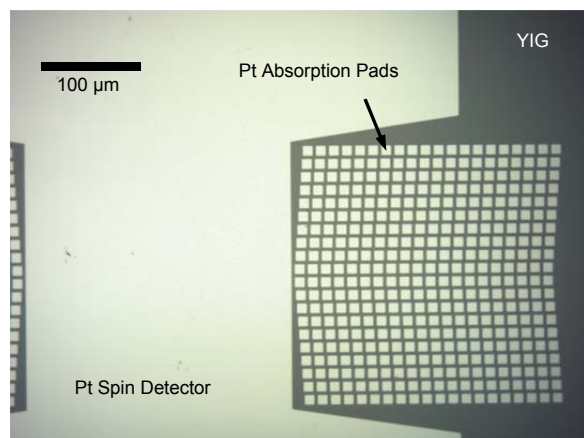
31. COMSOL Multiphysics® 4.4.
32. Suzuki, Y. & Tachibana, A. Measurement of the  $\mu\text{m}$  sized radius of a Gaussian laser beam using the scanning knife edge. *Appl. Opt.* **14**, 2809 (1975).
33. Kirillova, M. M., Nomerovannaya, L. V., & Noskov, M. M. Optical interband absorption in Platinum. *Phys. Met. Metallogr.* **34**, 51-57 (1972).
34. Kolobanov, V. N. *et al.* Reflectivity in yttrium iron garnet between 4 and 30 eV using synchrotron radiation. *Czech. J. Phys. B* **37**, 232-238 (1987) .
35. Rakić, A. D., Djurišić, A. B., Elazar, J. M. & Majewski, M. L., Optical properties of metallic films for vertical-cavity optoelectronic devices. *Appl. Opt.* **37**, 5271-5283 (1998).
36. S. H. Wemple, S. L. Blank, J. A. Seman, and W. A. Biolsi, *Phys. Rev. B* **9**, 2134 (1974).
37. Schreier, M. *et al.* Magnon, phonon, and electron temperature profiles and the spin Seebeck effect in magnetic insulator/normal metal hybrid structures. *Phys. Rev. B* **88**, 094410 (2013).
38. Jensen, J. E., Tuttle, W. A., Stewart, R. B., Brechnam, H. & Prodell, A. G. *BROOKHAVEN NATIONAL LABORATORY SELECTED CRYOGENIC DATA NOTEBOOK*, Vol. 1, Sec. VII (Brookhaven National Laboratory, New York, 1980).
39. Arblaster, J. W. The thermodynamic properties of Platinum on ITS-90. *Platinum Metals Rev.* **38**, 119-125 (1994).
40. Jiji, L. M., *HEAT CONDUCTION*, 3<sup>rd</sup> edn. (Springer-Verlag Berlin Heidelberg, Berlin, 2009).
41. White, G. K. & Woods, S. B. Electrical and thermal resistivity of the transition elements at low temperatures. *Phil. Trans. R. Soc. Lond. A* **251**, 273-302 (1959).
42. Foote, P.D. *Phys. Rev.* **4**, 550 (1914).

43. G. K. White and S. B. Woods, Philosophical Transactions of the Royal Society of London. Series A, Mathematical and Physical Sciences, Vol. 251, No. 995, (1959).
44. J. E. Jensen, W. A. Tuttle, R. B. Stewart, H. Brechna and A. G. Prodehl, Brookhaven National Laboratory selected cryogenic data notebook Vol. 1, Sec. VII (1980).
45. Kaviany, Massoud. Principles of Heat Transfer. Wiley-Interscience. June 7, 2001.

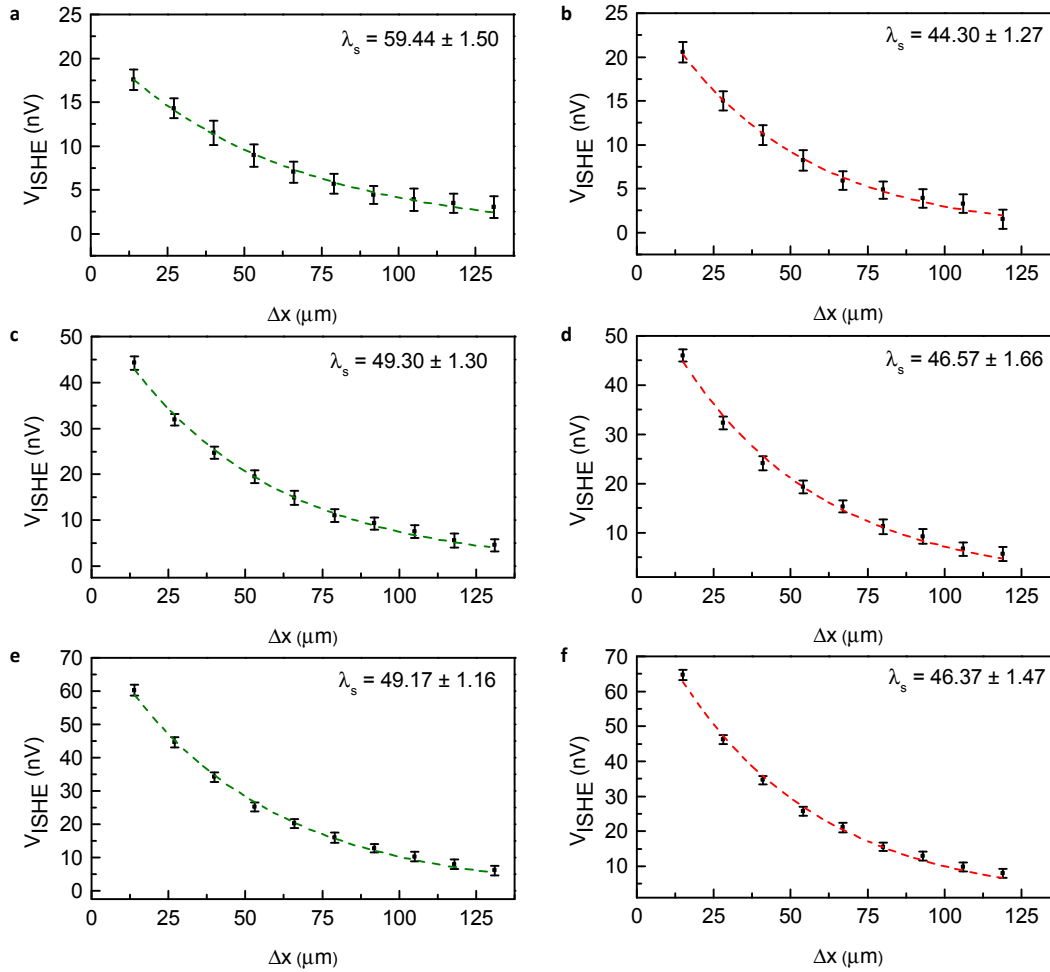
## Extended Data Figures



**Extended Data Figure 1 | Comparison of temporal (dark blue circle) and steady-state (dark blue dashed line) temperature profile at Pt/YIG interface.** The comparison is made along the optical axis heated by the laser power pulse train modulated at 2 kHz, with a power of  $3.2 \times 10^{16} \text{ W/m}^3$  at the Pt surface (red dashed line). A comparison of the temporal (light blue squares) and steady-state (light blue dashed line) temperature profile at a position of  $10 \mu\text{m}$  below the Pt/YIG interface is also shown.

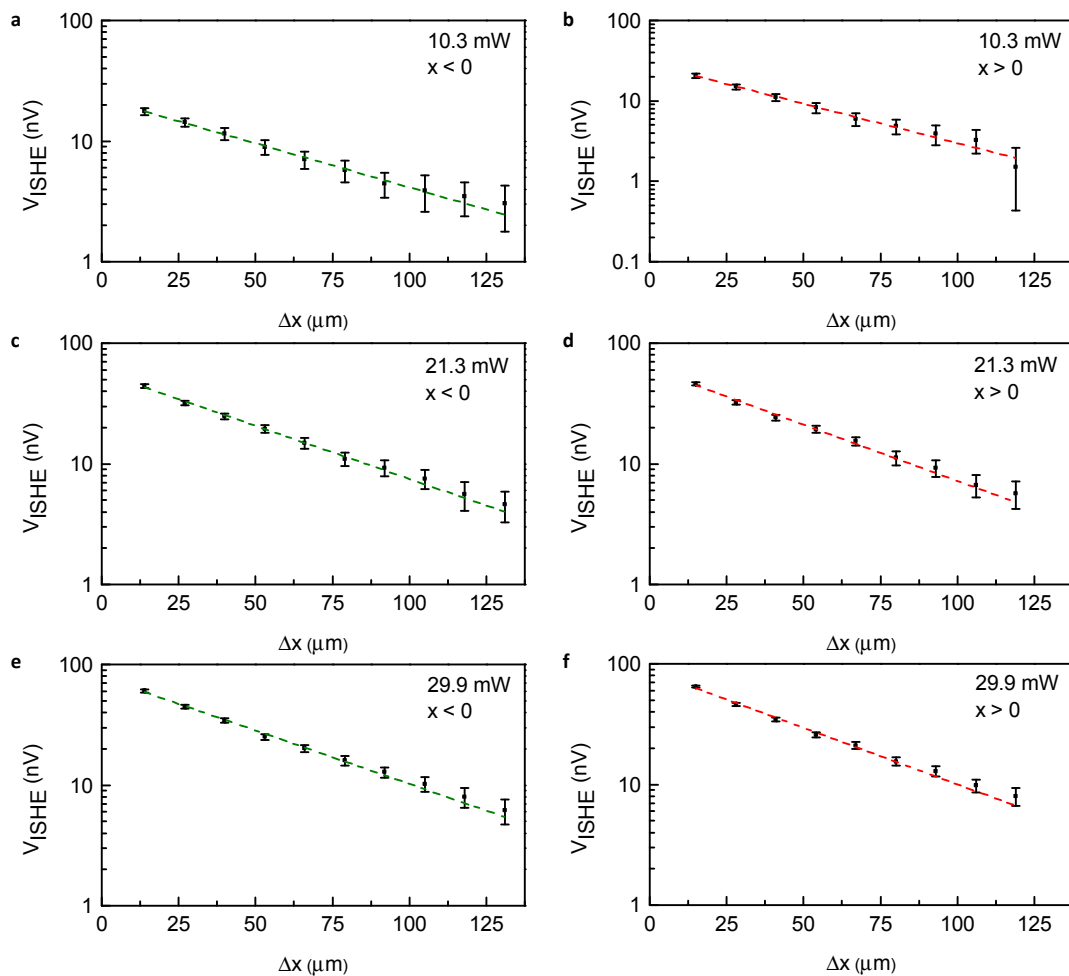


**Extended Data Figure 2 | Micrograph image of the processed non-local Spin Seebeck measurement device.** The  $265 \times 265 \mu\text{m}$  Pt spin detector is used to measure the spin current that diffuses laterally through the YIG after being thermally generated beneath one of the  $10 \times 10 \mu\text{m}$  Pt absorption pads.

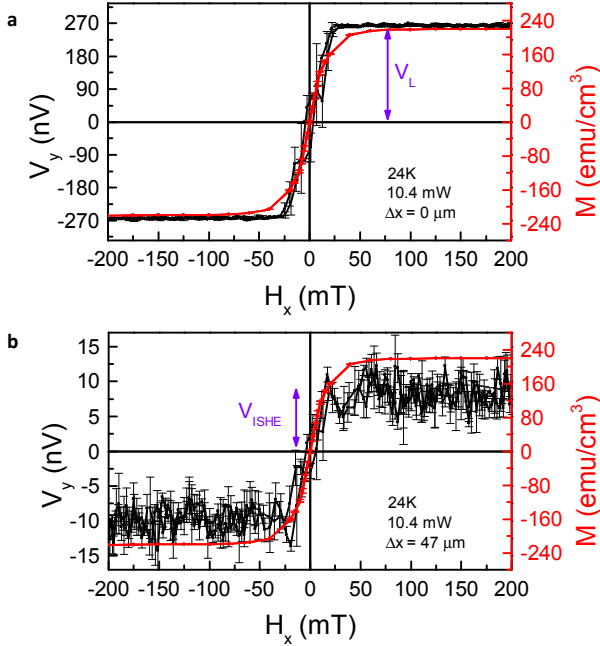


**Extended Data Figure 3 |  $V_{\text{ISHE}}$ , as a function of  $\Delta x$  for increasing laser power.**

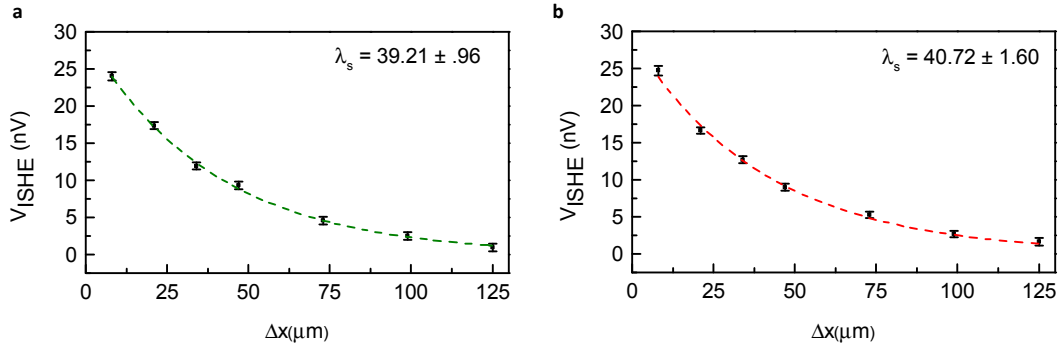
Laser powers are 10.5 mW (a), (b), 21.3 mW (c), (d), and 29.9 mW (e), (f). Green and red dotted lines correspond to the best fit single decaying exponential when the laser is to the left ( $x < 0$ ) or right ( $x > 0$ ) of the spin detector, respectively. Extracted spin diffusion lengths (in  $\mu\text{m}$ ) are shown in the corresponding figure panels. All measurements were performed at 23 K.



**Extended Data Figure 4 | Logarithmic plot of  $V_{\text{ISHE}}$ , as a function of  $\Delta x$  for increasing laser power.** Data from Extended Data Figure 3 plotted on logarithmic scale in order to emphasize the validity of a single exponential fit. The fits lie within error bars for all data points.



**Extended Data Figure 5 | Verification of non-local measurement on Sample 20141004. (a)**  $V_L$  is measured with the laser focused directly on the spin detector. The signal tracks the magnetization, following the same trends as seen on sample 20140804. **(b)**  $V_{\text{ISHE}}$  is measured with the laser on an absorption pad  $47 \mu\text{m}$  away. As seen in sample 20140804,  $V_{\text{ISHE}}$  is an order of magnitude smaller than  $V_y$ , and is attributed to diffusion of the magnon mediated spin current.



**Extended Data Figure 6 |  $V_{\text{ISHE}}$ , as a function of  $\Delta x$  on sample 20141004.** Laser power is 10.5 mW. Green and red dotted lines correspond to the best fit single decaying exponential when the laser is to the left or right side of the spin detector, respectively. Extracted spin diffusion lengths (in  $\mu\text{m}$ ) are shown in the corresponding figure panels. All measurements were performed at 24 K.

**Extended Data Table 1 | Refractive index ( $n$ ), reflectivity ( $R$ ), absorption coefficient ( $\alpha$ ), density ( $\rho$ ), thermal conductivity ( $\kappa$ ) and heat capacity ( $C$ ) used in the simulation.**

	$n$	$R$	$\alpha$ (1/m)	$\rho$ (kg·m <sup>3</sup> )	$\kappa$ (W·m <sup>-1</sup> ·K <sup>-1</sup> )	$C$ (J·kg <sup>-1</sup> ·K <sup>-1</sup> )
t	$1.89 + 4.54i$ <sup>31</sup>	73.2%	$78.3 \times 106$ <sup>31</sup>	21450 <sup>37</sup>	350 <sup>38</sup>	11.7 <sup>39</sup>
IG	$2.07 + 0i$ <sup>34</sup>	12.1%	0	5245 <sup>37</sup>	109.5 <sup>30</sup>	5.6 <sup>30</sup>

**Extended Data Table 2 | Decaying single exponential fit parameters as a function of laser power and laser position relative to the spin detector**

Power (mW)	Left Side ( $x < 0$ )			Right Side ( $x > 0$ )		
	$V_0$ (nV)	$\lambda_s$ ( $\mu\text{m}$ )	Adj $R^2$	$V_0$ (nV)	$\lambda_s$ ( $\mu\text{m}$ )	Adj $R^2$
10.5	$22.2 \pm .41$	$59.44 \pm 1.50$	.996	$28.5 \pm .70$	$44.30 \pm 1.27$	.996
21.3	$57.1 \pm 1.20$	$49.30 \pm 1.30$	.996	$61.2 \pm 1.69$	$46.57 \pm 1.66$	.994
29.9	$78.9 \pm 1.57$	$49.17 \pm 1.16$	.997	$86.7 \pm 2.34$	$46.35 \pm 1.47$	.995

\*Sample 20140804

Power (mW)	Left Side ( $x < 0$ )			Right Side ( $x > 0$ )		
	$V_0$ (nV)	$\lambda_s$ ( $\mu\text{m}$ )	Adj $R^2$	$V_0$ (nV)	$\lambda_s$ ( $\mu\text{m}$ )	Adj $R^2$
10.5	$29.4 \pm .48$	$39.21 \pm .96$	.998	$29.1 \pm .80$	$40.72 \pm 1.60$	.995

\*Sample 20141004

**Extended Data Table 3 | Comparison of the quality of single exponential fits to multiple data sets containing  $V_{ISHE}$  values from zone II and III and from zone III (Sample 20140804)**

Left Side ( $x < 0$ )			Right Side ( $x > 0$ )		
Power (mW)	Absolute value of $\Delta x$ ( $\mu\text{m}$ )	Adj $R^2$	Power (mW)	Absolute value of $\Delta x$ ( $\mu\text{m}$ )	Adj $R^2$
10.5	79 – 118	0.9323	10.5	80 – 119	0.99136
	66 – 118	0.96958		67 – 119	0.99618
	53 – 118	0.98175		54 – 119	0.97702
	40 – 118	0.98757		41 – 119	0.98384
	27 – 118	0.99469		28 – 119	0.99112
	14 – 131	0.99596		15 – 119	0.99451
21.3	79 – 118	0.97598	21.3	80 – 119	0.97851
	66 – 118	0.98487		67 – 119	0.99017
	53 – 118	0.99246		54 – 119	0.99556
	40 – 118	0.99696		41 – 119	0.99661
	27 – 118	0.99863		28 – 119	0.99801
	14 – 131	0.99622		15 – 119	0.99375
29.9	79 – 118	0.99882	29.9	80 – 119	0.99001
	66 – 118	0.99963		67 – 119	0.98997
	53 – 118	0.99981		54 – 119	0.99546
	40 – 118	0.9948		41 – 119	0.99657
	27 – 118	0.99629		28 – 119	0.99679
	14 – 131	0.99654		15 – 119	0.99581

\* Yellow regions refer to data sets with  $V_{ISHE}$  values from zones II and III. Purple regions refer to data sets containing  $V_{ISHE}$  values from zone III only.

**Extended Data Table 4 | Comparison of the quality of single exponential fits to multiple data sets containing  $V_{ISHE}$  values from zone II and III and from zone III (Sample 20141004)**

Power (mW)	Left Side ( $x < 0$ )		Right Side ( $x > 0$ )		
	Absolute value of $\Delta x$ ( $\mu\text{m}$ )	Adj $R^2$	Power (mW)	Absolute value of $\Delta x$ ( $\mu\text{m}$ )	Adj $R^2$
10.5	47 – 125	0.99724	10.5	47 – 125	0.99709
	34 – 125	0.99749		34 – 125	0.99391
	21 – 125	0.99876		21 – 125	0.99695
	8 – 125	0.99545		8 – 125	0.99843

\* Yellow regions refer to data sets with  $V_{ISHE}$  values from zones II and III. Purple regions refer to data sets containing  $V_{ISHE}$  values from zone III only.